PNAS RESEARCH ARTICLE | APPLIED PHYSICAL SCIENCES OPEN ACCESS

Geometrically programmed self-limited assembly of tubules using DNA origami colloids

Daichi Hayakawa[a], Thomas E. Videbæk[a], Douglas M. Hall[b], Huang Fang[a], Christian Sigl[c], Elija Feigl[c], Hendrik Dietz[c], Seth Fraden[a], Michael F. Hagan[a], Gregory M. Grason[b], and W. Benjamin Rogers[a,1]

Edited by Alexei Tkachenko, Brookhaven National Laboratory, Upton, NY; received May 6, 2022; accepted September 11, 2022 by Editorial Board Member Paul Chaikin

Self-assembly is one of the most promising strategies for making functional materials at the nanoscale, yet new design principles for making self-limiting architectures, rather than spatially unlimited periodic lattice structures, are needed. To address this challenge, we explore the tradeoffs between addressable assembly and self-closing assembly of a specific class of self-limiting structures: cylindrical tubules. We make triangular subunits using DNA origami that have specific, valence-limited interactions and designed binding angles, and we study their assembly into tubules that have a self-limited width that is much larger than the size of an individual subunit. In the simplest case, the tubules are assembled from a single component by geometrically programming the dihedral angles between neighboring subunits. We show that the tubules can reach many micrometers in length and that their average width can be prescribed through the dihedral angles. We find that there is a distribution in the width and the chirality of the tubules, which we rationalize by developing a model that considers the finite bending rigidity of the assembled structure as well as the mechanism of self-closure. Finally, we demonstrate that the distributions of tubules can be further sculpted by increasing the number of subunit species, thereby increasing the assembly complexity, and demonstrate that using two subunit species successfully reduces the number of available end states by half. These results help to shed light on the roles of assembly complexity and geometry in self-limited assembly and could be extended to other self-limiting architectures, such as shells, toroids, or triply periodic frameworks.

self-assembly | self-limited assembly | colloids | DNA origami | addressable assembly

Significance

Nature is replete with self-assembled materials that have one or more self-limited dimensions, including shells, tubules, and fibers. Despite significant advances in making nanometer- and micrometer-scale subunits, the programmable assembly of similar self-limiting architectures from synthetic components has remained largely out of reach. In this article, we create geometrically programmed subunits using DNA origami and study their assembly into tubules with a self-limited width. We show that the average self-limited dimension can be tuned by changing the local curvature encoded in a single subunit. Exploiting the programmability of our system, we further test the tradeoffs between fidelity and complexity embodied by two paradigms for self-limited assembly: self-closure through programmed curvature and addressable assembly through programmed specific interactions.

Self-assembly is a fundamental building principle used by Nature to make functional materials, including virus capsids for encapsulation and delivery (1, 2), cytoskeletal filaments for transport (3–5), and macromolecular machines with diverse roles, like the ribosome for protein synthesis (6). Recently, there has been considerable effort aimed at mimicking biological self-assembly to synthesize user-prescribed structures from synthetic nanometer- and micrometer-scale particles. For example, by encoding short-range specific interactions, DNA-grafted colloidal particles can be programmed to assemble into a variety of two- and three-dimensional crystal phases with prescribed symmetry groups and lattice constants (7–10). However, rather than unbounded crystal phases, the aforementioned biological functionalities—encapsulation, motility, and protein synthesis—arise from self-limiting structures that have one or more self-limited length scales.

How does one go beyond periodic lattice structures with macroscopically uncontrolled dimensions, to program the assembly of self-limiting architectures that have self-limited length scales that are arbitrarily large with respect to the size of the individual subunits (11)? There are two prominent paradigms for prescribing self-limited assembly: 1) addressable assembly and 2) self-closing assembly. In addressable assembly, every component of a multispecies ensemble is distinct and is programmed to occupy a specific location within a target structure (12–14). Therefore, increasing the self-limited length scale necessitates increasing the assembly complexity in terms of the number and interaction specificity of the subunits. In self-closing assembly, anisotropic interactions give rise to the accumulation of curvature during growth that causes the structure to self-close at a finite size (11). In contrast to addressable assembly, the self-limited length scale in self-closing assembly is therefore controlled by the binding angles between neighboring subunits and is programmed geometrically rather than through specific interactions and, as such, may require only one or relatively few subunits to target a specific self-closing size. But which strategy should one select for a particular target geometry, and which approach is more accurate, precise, or economical? Because the vast majority of examples either address only one paradigm or do not distinguish between the two, as in DNA-coated colloids (15), DNA tiles (16–19), hierarchical assembly of DNA origami (20–24), and designed

Author contributions: D.H., D.M.H., G.M.G., and W.B.R. designed research; D.H. and T.E.V. performed research; D.H., T.E.V., H.F., and E.F. analyzed data; D.H., T.E.V., D.M.H., H.F., C.S., E.F., H.D., S.F., M.F.H., G.M.G., and W.B.R. wrote the paper; T.E.V., H.F., and M.F.H. developed the theory; and D.H., C.S., H.D., S.F., G.M.G., and W.B.R. designed the DNA origami.

The authors declare no competing interest.

This article is a PNAS Direct Submission. A.T. is a guest editor invited by the Editorial Board.

[1]To whom correspondence may be addressed. Email: wrogers@brandeis.edu.

This article contains supporting information online at https://www.pnas.org/lookup/suppl/doi:10.1073/pnas.2207902119/-/DCSupplemental.

Published October 17, 2022.

proteins (25, 26), direct comparisons between addressability and geometry in prescribing self-limited assembly are obscured.

In this article, we create an experimental platform using DNA origami for examining the roles of geometric and interaction specificity in arguably the simplest system that could in principle be programmed by geometry alone: the assembly of cylindrical tubules from rigid triangular monomers. The tubule is the ideal target geometry because it represents an infinitely large class of structures, each of which can be assembled from a single subunit species by controlling the dihedral angles between neighboring subunits. As anticipated, we show that we can vary the self-limited width of the tubules by tuning the dihedral angles between neighboring subunits without changing the interaction complexity. However, we find that the width of the assembled tubules takes a range of values and that the distribution broadens upon increasing the mean tubule width. We discuss how this distribution of the self-limited width is a generic feature of self-closing assembly when the self-limited length scale is sufficiently large compared to the size of the building block (27), which we understand using a simple theory. We conclude by exploring how increasing the assembly complexity enables us to constrain the width distribution by using multiple species of triangles with increased numbers of specific interactions. For a binary mixture of triangle species, we validate that the allowed states of the assembled tubules are reduced by half, as expected from simple geometrical arguments.

1. Results and Discussion

A. Design Principles. Our system consists of rigid triangular subunits made by DNA origami (24) that encode all of the information necessary to self-assemble tubules with user-prescribed geometries (Fig. 1*A*). Assembling tubules from triangular subunits requires that we specify two types of information: 1) the interaction specificity between the edges and 2) the local curvature between neighboring subunits. We encode the specific interactions by using unique protrusions and recesses that give rise to shape-complementary lock-and-key interactions whose attraction originates from blunt-end stacking (Fig. 1*B*) (28). At a

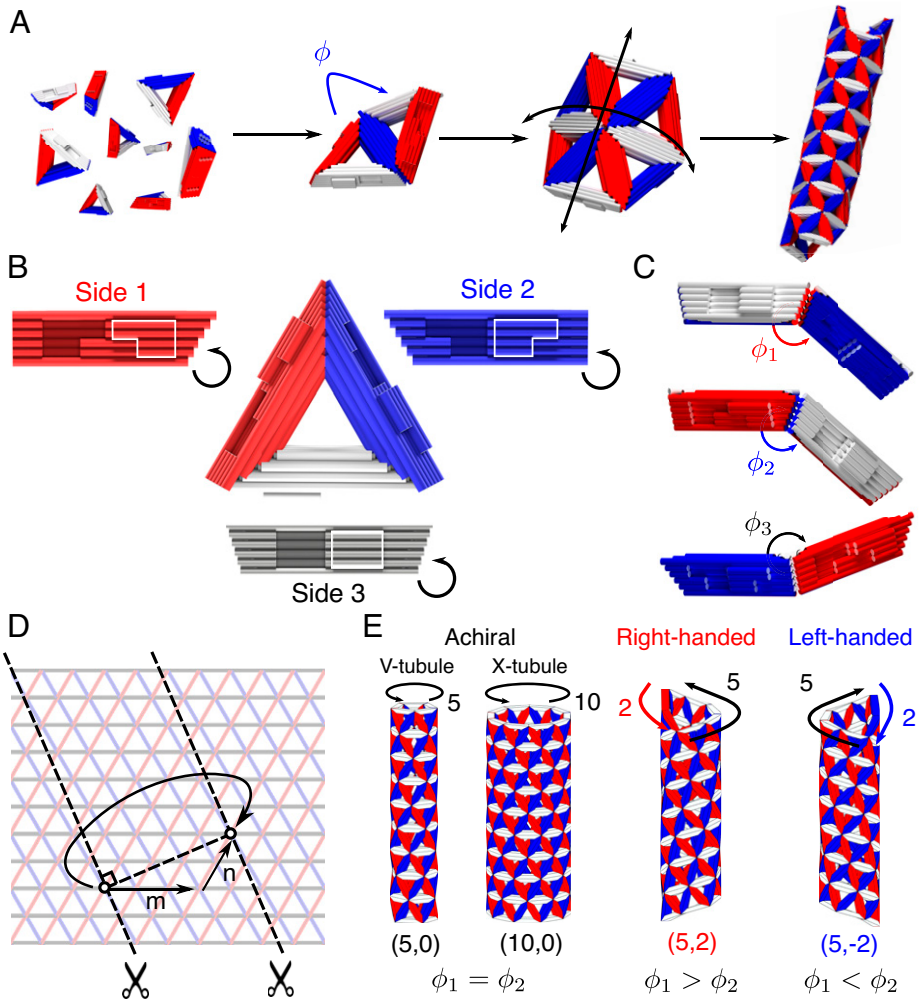

Fig. 1. Overview of the design rules for tubule assembly. (*A*) Triangular subunits bind at the edges with dihedral angles ϕ that specify the principal curvatures of the assembly to favor the formation of cylindrical tubules. (*B* and *C*) Design principles of triangular subunits assembling into tubules. (*B*) Each side has self-complementary lock-and-key interactions encoded in shape-complementary protrusions and recesses. Holes on the faces are shaded, while protrusions are highlighted with white. Black arrows indicate the sides that bind together. In this case, each side binds to itself. The subunits have edge lengths of 56 nm; each side has a width of 10 nm and a height of 15 nm. (*C*) The sides are also beveled so that when two triangles bind, they form a unique dihedral angle ϕ that is determined by the bevel angle. (*D*) A triangular lattice that is cut along two parallel lines can be rolled into a tubule, with periodicity determined by indexes *m* and *n*. *m* denotes the number of steps along side 3, while *n* is the number of steps along side 1 or 2 (if $n > 0$, it is side 1, and if $n < 0$, it is side 2). (*E*) Any tubule is identified by an index pair, (m, n). V tubule and X tubule, corresponding to (5,0) and (10,0), are achiral tubules with 5 and 10 triangles in circumference, respectively. Tubules of varying width and chirality can be assembled by tuning the magnitudes of the dihedral angles ϕ_1, ϕ_2, and ϕ_3. For the size of subunits shown here, (5,0) and (10,0) tubules have wall thicknesses of 15 nm and cavity diameters of ~60 nm and 150 nm, respectively.

minimum, we require three specific interactions—one per side—which are each homophilic. These three specific interactions allow the triangular subunits to assemble into a deterministic triangular lattice, where each side aligns with one of the three lattice directions.

Additionally, we encode the local curvature by specifying the dihedral angles between neighboring subunits. Specifically, we bevel each side of the triangular subunit, such that it forms the three dihedral angles with its three neighbors (Fig. 1*C*). Here, the bevel angle is given by θ_B as $(\pi - \phi)/2$, where ϕ is the dihedral angle. The unique combination of the three dihedral angles can be assigned to target a tubule geometry. For example, the subunit in Fig. 1 *B* and *C*, which assembles into a tubule with five subunit edges in circumference, has dihedral angles of 138.2, 138.2, and $-158.4°$ for sides 1, 2, and 3, respectively. The accumulation of curvature from the dihedral angles upon assembly results in the formation of a curved triangular lattice. For appropriately chosen angles, the lattice will close upon itself to form a tubule (Fig. 1*D*), which can be chiral or achiral depending on how the tubule closes (Fig. 1*E*). See *SI Appendix*, section 2 for more details of the tubule geometry.

Because the curvature originates from the combination of three bevel angles, the width, handedness, and pitch of the resulting tubules can be programmed using these three angles alone. Indeed, the final tubule structure is equivalent to the equilateral Yoshimura pattern of a buckled cylindrical shell (29), which constitutes a class of origami tilings of cylinders via a single triangular facet with a single set of fold angles on its three edges. In the case of tubules, larger dihedral angles in the direction perpendicular to the tubule axis produce wider tubules. Furthermore, setting the dihedral angles of sides 1 and 2 to different values produces chiral tubules with different pitch and handedness (Fig. 1*E*). The relative magnitude of the two dihedral angles determines the handedness and the difference between the two angles determines the pitch, with a larger difference leading to a larger pitch. Thus, by tuning the dihedral angles of the three sides, we can assemble a variety of different tubule structures. We note that the ability to program any tubule geometry using a single triangular facet is in contrast to the ability to program assembly of an icosahedral shell, for example, which requires a larger and larger number of unique facets upon increasing the shell diameter (1, 24).

The resulting tubules can be uniquely classified using a pair of lattice indexes, (m, n) (30). Here, m refers to the vector along side 3 of the triangle and n refers to the vector along side 1 ($n > 0$) or side 2 ($n < 0$). Therefore, (m, n) defines the shortest distance along the triangular lattice to go around the tubule and come back to the same vertex. Note that we consider only the case $m \geq |n|$. With our convention, we use the positive index n to define right-handed tubules and the negative index n for left-handed tubules. Each tubule type is associated with a different set of dihedral angles for the three sides.

B. Tubule Assembly. To demonstrate the utility of our experimental approach, we design two different monomers that assemble into tubules with different widths: V triangle, which targets a (5,0) tubule, and X triangle, which targets a (10,0) tubule (Fig. 2*A*).* Each side of the triangle has a cross-section that is 4×6 double helices arranged on a square lattice (*SI Appendix*, Fig. S3*A*). We specify the three unique bevel angles required for a particular tubule geometry by varying the relative lengths of the double helices (*SI Appendix*, Fig. S3*B*). We encode the specific shapes of the protrusions and recesses by designing the scaffold routing, which we choose to disallow off-target binding and to enforce the correct relative orientations of neighboring subunits. The size of the subunits is set by the length of the DNA scaffold, which is 8,064 nucleotides long. See *SI Appendix*, section 3 for details of the subunit design.

We fold, purify, and assemble the subunits using standard DNA origami protocols. In brief, we fold the origami using a slow, linear temperature ramp, purify the resulting monomers by gel extraction, and then assemble them at constant temperature for 1 wk in a rotating incubator (31) (*SI Appendix*, section 5). For a given design, we perform multiple assembly experiments at different concentrations of $MgCl_2$ to tune the strength of the intersubunit attraction. Finally, we characterize the structures of the individual monomers using single-particle cryogenic electron microscopy (cryo-EM) (32) and the entire assemblies using negative-stain transmission electron microscopy (TEM).

The bevel angles of the folded monomers are close to the target values but do not match them exactly. By fitting a pseudoatomic model to our cryo-EM reconstructions (33) we make an estimate of the bevel angles of each of the three sides for both of our monomers (Fig. 2*A*). We find that for the V triangle the three sides have angles of $(21.3 \pm 0.1, 21.3 \pm 0.1, -5.5 \pm 0.1)$ compared with the target angles of $(20.9,\ 20.9,\ -10.8)$. Comparing these angles to the angles of different tubule types, this monomer is closest to a (5,0) tubule, as designed.† In contrast, for the X triangle, we see monomer bevel angles of $(11.4 \pm 0.1, 9.0 \pm 0.1, -6.4 \pm 0.1)$ compared with $(10.4, 10.4, -5.2)$, yielding a closest predicted state of a $(9, -1)$ tubule. While the $(9, -1)$ tubule has a similar diameter to the (10,0) one, it is chiral and left handed rather than achiral, as in the designed monomer. See *SI Appendix*, section 8 for more details on the cryo-EM reconstructions.

The assembly of the triangular subunits into self-limiting structures depends on the intersubunit attraction, which can be controlled by varying the concentration of $MgCl_2$. For both designs, we observe the same sequence of outcomes upon increasing the Mg^{2+} concentration (Fig. 2*B*). At low Mg^{2+} concentration, we observe only monomers and oligomers containing a few subunits. At intermediate Mg^{2+} concentration, we see the assembly of filament-like, self-limited structures in coexistence with monomers. Given that we observe the coexistence of assemblies and monomers, we hypothesize that the assembly occurred near to equilibrium and that growth occurred by monomer addition. However, we note that additional experiments are required to test this hypothesis and uncover the detailed kinetic pathways to assembly. At higher Mg^{2+} concentrations, we observe large disordered aggregates and rarely observe monomers or small clusters. Therefore, we hypothesize that these large aggregates are likely due to kinetic arrest (34). While these results are consistent with previous measurements of the stacking interactions between blunt ends, which show that the interactions become stronger upon increasing Mg^{2+} concentration (35), we highlight that our experimental estimates of the binding free energies per side differ by roughly a factor of 2 from the sum of all of the stacking energies (*SI Appendix*, Table S2). Therefore, given the importance of the binding free energy in the assembly outcome, experimental techniques to directly measure the binding free energies, as well as more complete models of these types of lock-and-key interactions, are needed.

*Roman numerals V and X are used as shorthand for the target tubule types (5,0) and (10,0), respectively.

†The closest state is the tubule type whose bevel angles have the minimum distance in quadrature from the measured angles.

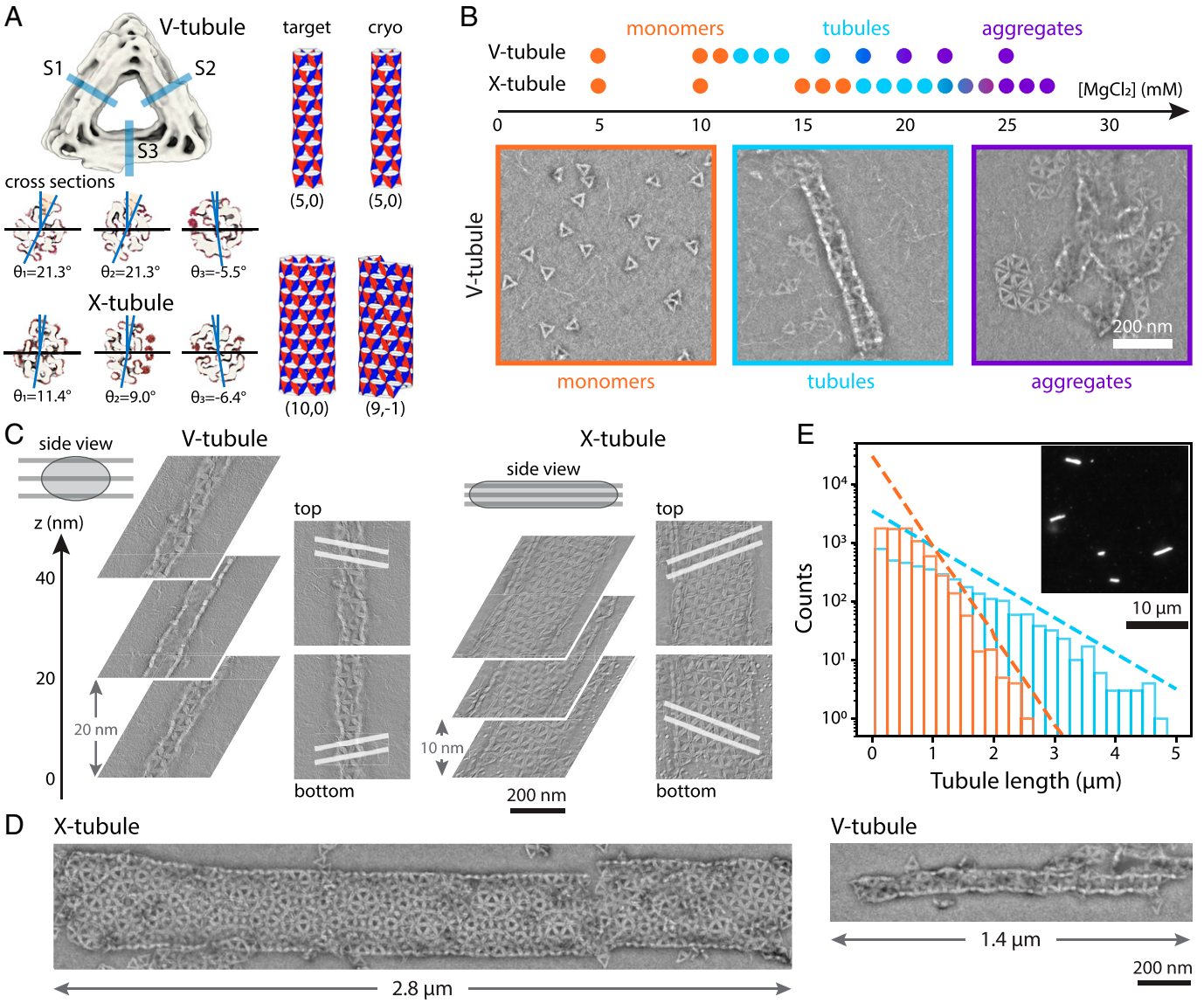

Fig. 2. Self-assembly of tubules. (*A*) Cryo-EM single-particle reconstructions for V triangle and X triangle. Shown are cross-sections of three sides of the triangles (gray) and the estimated bevel angles, θ, from fitting the cryo-EM reconstruction to a pseudoatomic model (maroon) (*SI Appendix*, section 8). Tubule illustrations show the target geometry (labeled target) and the expected tubule geometry predicted from our cryo-EM measurements (labeled cryo) for the V tubule and the X tubule. (*B*) Negative-stain transmission electron micrographs of V triangles after incubation at different $MgCl_2$ concentrations for 1 wk at 40 °C. The points above the images show the $MgCl_2$ concentrations that lead to assembly of monomers (orange), tubules (cyan), or aggregates (purple). (*C*) Tomography reconstructions of the V and X tubules, showing different *z* positions. The orientation of side 3 is illustrated with white lines. (*D*) Images of tubules observed with V triangles (*Right*) and X triangles (*Left*). For the X tubule one can see a Moiré pattern where the tubule has closed on itself. (*E*) Histograms of the tubule length observed with epifluorescence for V tubules (orange) and X tubules (cyan). Note that the length distribution combines statistics from tubules with different lattice numbers. Dashed lines are guides for the eye to highlight the exponential decay in length (*SI Appendix*, section 7.A). *Inset* shows an example fluorescence image.

TEM tomography confirms that the filament-like structures are indeed tubules. First, we observe a single filament assembled from V triangles (Fig. 2*C*). Looking at different slices through the filament in the direction normal to the EM grid, or *z* stack, we see that the structure clearly shows two triangular lattices at different *z* positions, separated by a hollow core. The distance between the top and bottom lattices is around 40 nm, which is shorter than the expected diameter of 88 nm, but longer than 20 nm, or twice the thickness of a triangle. Therefore, we hypothesize that the cross-section of the tubule deposited on grid is elliptical. Finally, we also see that the top and bottom lattices have different orientations of the triangular lattice with respect to one another, as would be expected for a chiral tubule. Taken together, these observations confirm that the filament is indeed a tubule. Going further, the lattice orientation can be tracked around the tubule, yielding a (4,1) tubule for this case. While this determination gives us only the magnitude of n, we also determine the handedness by comparing our reconstructions to reconstructions of a DNA origami nanohelix labeled with gold nanoparticles in a right-handed, chiral arrangement (*SI Appendix*, section 7.B) (36, 37).

Similarly, we find that the wider filaments formed from X triangles are also tubules. As with the V triangles, the tomograms of the wide filaments show two triangular lattices, which are mirror images of one another and spaced apart along the *z* direction. In this case, the distance between the bottom and the top lattices is around 20 nm, which matches the height of two triangles. We suspect that this spacing is due to the flattening of the X tubule during the sample preparation. This hypothesis is further supported by the observation that the two triangular lattices appear to be planar, as expected for a flattened tubule. Finally, similar

to the example V tubule, the specific X tubule shown in Fig. 2*C* is also chiral and right handed, as seen in the mirror reflection of the top and bottom lattices (*SI Appendix*, section 7.B).

Remarkably, we find that both V tubules and X tubules can grow to micrometers in length and exhibit length distributions that are characteristic of equilibrium one-dimensional growth. Fig. 2*D* shows examples of some of the longest tubules that we observe in electron microscopy for both designs. The V tubule is roughly 1,200 nm in length and is made from about 210 subunits. The X tubule is nearly 3 μm long and is assembled from about 1,400 subunits. To complement our EM observations, we also perform epifluorescence microscopy experiments to get a more complete view of the tubule lengths (Fig. 2*E*) (see *SI Appendix*, section 7.A for details). We find that both V and X tubules are characterized by length distributions that decay exponentially, with means of 0.5 and 0.9 μm, respectively, which are consistent with expectations for equilibrium one-dimensional assembly (38). In the extremes, we find assemblies reaching up to 5 μm in length. Comparing our X-tubule results to earlier attempts to assemble tubules of similar width from DNA origami subunits (23) shows that our approach yields assemblies that are roughly an order of magnitude longer and contain about five times the number of subunits. Furthermore, our results show that although the width of the tubule is self-limited, the tubule lengths are unconstrained.

C. Tubule Distributions. Whereas the results above show the structure of single tubules, our assembly experiments yield an ensemble of tubules that exhibits a variety of widths and lattice orientations, despite being formed from a single monomer type. For both the V- and X-tubule designs, we identify the pair of indexes (m, n) that classifies the structure for each of hundreds of individual tubules observed under TEM and create a distribution (Fig. 3*A*). The distribution shows that the most probable tubule types are (4,0) and (9,4) for the V and X tubules, respectively, with the probability of different states falling off with distance from this tubule type. Furthermore, we find that the breadth of the X-tubule distribution is larger than that of the V-tubule distribution. Although we cannot easily determine the chirality of every tubule, we examined 13 chiral V tubules and 15 chiral X tubules using tomography. In both cases, all of the tubules that we examined were right handed. See *SI Appendix*, sections 7.B and 7.C for a detailed description of the tubule classification.

The observed distributions beg two important questions: 1) Why are the tubule distributions not centered around the target structures? And, 2) What determines the breadth of the tubule distribution around the most probable tubule type? We address the first question by returning to our single-particle reconstructions of the monomers from cryo-EM (Fig. 2*A*). While the bevel angles of the cryo-EM map for the V triangle predict a tubule state of (5,0), which is close to the peak of the experimental distribution, (4,0), the X-triangle prediction of (9,−1) is 13% narrower in width than the (9,4) peak that we observe. We note that the cryo-EM map of the X triangle shows that some parts of the lock-and-key design protrude from the structure due to a missed cross-over in the origami design (*SI Appendix*, Fig. S18). Therefore, we hypothesize that this aspect of the structure causes a poor fit for the lock-and-key shapes of the interaction, leading to unintended torques that could skew the dihedral angles to a different value. This misfit would cause a shift in the mean of the distribution away from what is expected from the geometry of the monomer alone.

Next, we tackle the origin of the breadth of the distribution. We start by noting that tubules with neighboring lattice numbers

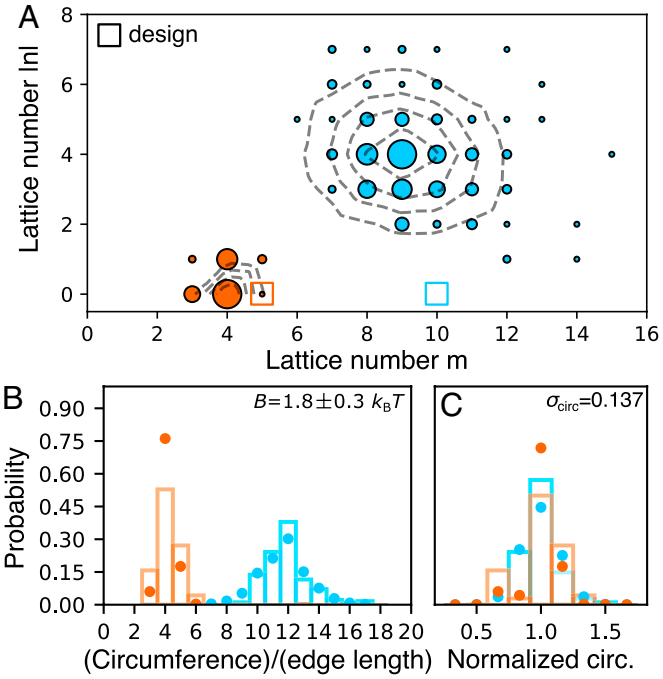

Fig. 3. Measured distributions of the lattice numbers of observed tubules. (*A*) Lattice number distribution of the two tubules. The size of each circle is proportional to the number of tubules found for that lattice number. Orange represents data for the V tubule, while cyan represents data for the X tubule. The square symbols denote the target states. Contours show the expected spread based on model predictions, described in the text, where the spacing between contours is 20% of the peak probability. The plot shows distributions from $n = 70$ and $n = 182$ tubules for V and X tubules, respectively. (*B*) Histograms of the measured circumferences of the tubules. Points come from a model prediction using a bending rigidity of $B = 1.8 \pm 0.3\ k_BT$; bars show experimental data. (*C*) The corresponding distributions of the circumferences normalized by the mean, whose variance, σ^2_{circ}, is used to estimate B. $\sigma_{circ} = 0.137$ is the average of the SDs obtained from the V- and X-tubule distributions.

vary only by small changes in their dihedral angles. Therefore, if the bending rigidity of the assembly is sufficiently small, thermal fluctuations will cause the dihedral angles between neighboring triangles to explore a range of possible values, leading to tubules with larger or smaller diameters.

This idea can be captured by considering the Helfrich energy of an elastic sheet, $E_H = \frac{1}{2}BA(\Delta\kappa_\perp)^2$, where A is the surface area, B is the bending rigidity, and $\Delta\kappa_\perp$ is the fluctuation of the sheet's curvature in the circumferential direction (39). We assume that as the assemblies grow, they must first form a patch-like circular sheet before closing into a tubule. Thermal fluctuations will cause this sheet to accommodate different curvatures from its preferred value, but once it grows large enough to close into a tubule, we assume that it cannot open into a sheet again, thereby locking in a specific tubule circumference. If the growth rate is faster than the dissociation of a subunit–subunit bond, then once a tubule forms and starts to grow, the possibility of opening a large number of bonds to allow the tubule to reform into a different type becomes increasingly unlikely. Therefore, we estimate the size of assemblies at this closure point as a disk with a diameter that corresponds to the circumference of the closed tubule. The fluctuations of the sheet's curvature at the point of closure will inherently lead to a distribution of tubule circumferences. Under these assumptions, we can write the Helfrich energy for a tubule at closure as

$$E_H = \frac{1}{2}B\pi^3\left(\frac{\Delta C}{C}\right)^2, \qquad [1]$$

where C is the circumference of a tubule. Assuming that the circumferences follow a Boltzmann distribution, $P \sim \exp(-E_{\mathrm{H}})$, we can relate the spread of the widths to the bending rigidity (27) (see *SI Appendix*, section 9 for details).

The predictions from the Helfrich energy are consistent with our experimental observations, suggesting that the width distribution is determined by the bending rigidity of the growing assembly and the irreversibility of closure. Fig. 3*B* shows the distribution of the tubule circumference for both V and X tubules. Following the insight we gained from considering the Helfrich energy, we rescale the circumference by the mean circumference of each distribution. Fig. 3*C* shows that for both V and X tubules the scaled distributions have similar breadths, with SDs of 0.149 and 0.125, respectively. The importance of this observation is that it is an inherent feature of self-closing assemblies at finite temperature: Whenever the assembly has a finite bending rigidity, the system will form a distribution of end states with a breadth that depends on the self-limited length scale relative to the size of the subunit.

Using the variance of the width distributions, we make an estimate of the bending rigidity of the V and X tubules. Assuming both assemblies have the same bending rigidity, we find $B = 1.8 \pm 0.3\ k_{\mathrm{B}}T$. Interestingly, the bending modulus that we find is orders of magnitude smaller than a naive estimate from the "worm-like" bundle model (40), which predicts that the elastic stiffness of the edges of triangles in a tubular assembly is of the order of 10^3 to $10^4\ k_{\mathrm{B}}T$, suggesting that flexibility of the intersubunit connections plays a dominant role. We can also use our measured bending rigidity as an input to perform more detailed energetics calculations (*SI Appendix*, section 9) to get a complete (m, n) distribution for the expected tubules (27), which is shown in the contours of Fig. 3*A*. Similarly, we can compute the circumference distributions for the model. In both cases, we find that our model predictions match the experimental data well (Fig. 3*B*), further supporting the idea that the distribution of tubules we observe in the experiment is due to finite bending rigidity and is therefore expected for self-closing structures. We note that an even more sophisticated computational model of tubule assembly predicts a bending modulus of roughly $B = 10\ k_{\mathrm{B}}T$ (41), slightly higher than our simple model, but still only different by a factor of 5.

D. Pruning the Tubule Distribution by Increasing the Assembly Complexity. Our observations of the X-tubule assembly highlight an inherent challenge in using self-closing assembly alone to target finite-sized soft materials: As we target larger self-closing lengths, the distribution of the self-limited dimension also gets broader. So how do we overcome this challenge to assemble wider tubules without compromising the accuracy of the assembly?

Here we turn our attention toward the other paradigm for encoding self-limitation: addressable assembly. The rationale of this approach is relatively easy to understand. By increasing the number of particle species per structure, and therefore the total number of specific interactions, the location of any given particle within that structure becomes more precisely defined. In the fully addressable limit, each particle species can only occupy a single position within the final structure while simultaneously maximizing the number of its favorable interactions. Therefore, by eliminating the other ways in which the particles can be arranged, the yield of the target assembly can be increased.

We explore this approach by assembling a (10,0) tubule from two unique species of triangular subunits. Fig. 4 shows our specific realization of this concept using a binary tiling that is compatible with tubule self-assembly (Fig. 4*A* and *SI Appendix*, section 4). The two species are placed periodically and unidirectionally in the pattern. Since each side encodes a specific dihedral angle, the sides must always remain in the same orientation. As before, a triangular lattice of these two species can be rolled up into a (10,0) tubule. However, unlike before, the binary lattice contains two distinct types of vertices. As a result, the assembled tubules have an additional constraint: When the triangular lattice closes to form a tubule, the closing vertices must match. Therefore, for our specific case, we expect that only tubules with an even lattice number n can assemble. The specific implementation of the lock-and-key geometries and their interactions is shown in Fig. 4*B* and the expected assembly is shown in Fig. 4*C*.

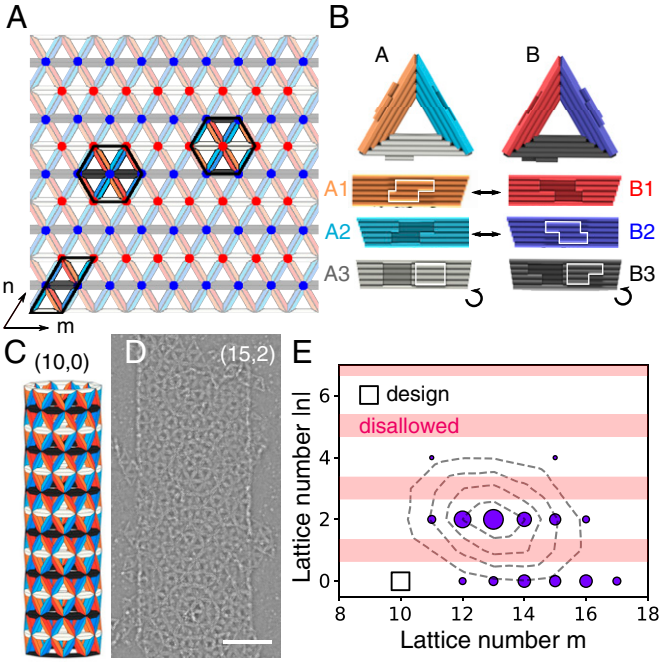

Fig. 4. Schematics for binary species tubules and their lattice number distributions. (*A*) Triangular tiling using two types of monomers. The highlighted region in the lower left shows the primitive cell of the tiling. Red and blue dots denote the two distinct vertices present in the pattern, which are highlighted as well. (*B*) Schematic representation of the two types of monomers we use to construct the tubule. Black arrows represent the binding pairs of the lock-and-key interactions. (*C*) Diagram of the intended (10,0) tubule structure. (*D*) Negative-stain TEM micrograph of a tubule made from the two species, whose tubule type is (15,2). (Scale bar, 200 nm.) (*E*) Tubule type distribution of the binary mixture. The size of each circle is proportional to the number of tubules found for that pair of lattice indexes. The square symbol denotes the target state. Contours show the expected spread based on model predictions with $B = 3.1\ k_{\mathrm{B}}T$, where the spacing between contours is 20% of the peak probability. This B value is estimated in the same manner as described previously. Red regions are disallowed due to the tiling pattern of the binary species, as seen in the experiments. The plot shows distribution from $n = 113$ tubules.

The distribution of assembled tubules demonstrates that increasing the assembly complexity limits the accessible states. Fig. 4*D* shows an example tubule and Fig. 4*E* is the tubule distribution that we measure. We find that the distribution is maximal at (13,2), with some tubules being chiral and others achiral. All seven tomography reconstructions of chiral tubules were identified to be right handed (*SI Appendix*, section 7.B). Most importantly, we do not find a single tubule classified by an odd value of n, as we intended by our design. We also find that the probability of the most common state is increased compared to what it would be with a single particle type. The binary assembly has a larger average circumference than the X tubule, which would suggest that the probability for the most common state would be comparatively lower. However, we find that the most populated state for the binary assembly is 22.1% compared to 17.6% for the X tubule.

This increase in probability is a result of using more species of triangles for the assembly since some fraction of tubules that might have had an odd n are distributed to nearby even n states.

As before, although the distribution is not centered around the target state, it has a width that is consistent with our energetics model. We hypothesize that the shift in the center of the distribution is again due to the experimental design challenge of accurately encoding the dihedral angles in our DNA origami subunits. The bevel angles of the triangles are designed to target X tubules, similar to the previous case. However, cryo-EM reconstructions of the individual subunits reveal bevel angles that predict a (13,−1) tubule (*SI Appendix*, section 8).

2. Conclusion

In summary, we devised a versatile class of colloidal particles using DNA origami and studied the roles of geometry and interaction complexity in their self-limited assembly into tubules. Our DNA origami design scheme allows for control over the valence, interaction specificity, and local curvature of the subunits, independently. We demonstrate that the DNA origami colloids enable the assembly of complex structures, such as tubules, with self-limited dimensions that are much larger than the individual subunits. Using this design principle, we designed and assembled tubules of different widths, demonstrating that information encoded in the geometry of individual subunits can be used to program the geometry of the entire assembly. However, due to the intrinsic flexibility of the binding, tubules with a variety of widths and chiralities assembled from the same subunits, which was especially prominent for wider tubules. Such a distribution of assembled tubules for a single monomer type is an inherent feature of bending fluctuations in curvature-limited assemblies.

Here, we experimentally demonstrated one path toward removing off-target structures to focus the distribution on the target of interest. The precision in reaching a specific state can be increased by combining interaction specificity with geometric specificity in a multispecies design. As one specific realization of this concept, we assembled tubules using two species of subunits, which effectively reduced the number of accessible states by half. Therefore, as more species of subunits are added to the system, we anticipate that the yield of the target state will increase, although likely at the cost of longer timescales for assembly (27). Another possibility other than interaction specificity that follows from our observations is that one can exploit the geometric specificity of the system to mitigate the formation of off-target structures. For example, designing ever more rigid binding sites should increase the energetic cost to deform the structure away from the target geometry. While it is not clear how much control there is over this aspect given the material properties of the subunits themselves, one might expect the bending rigidity to vary with the particle aspect ratio (i.e., thickness to width) based on elastic considerations alone. Finally, Nature, confronted with the same design challenge of assembling tubules from few components, has evolved a third strategy for eliminating off-target states: employing seeded nucleation, as seen with the in vivo assembly of microtubules (3, 42, 43). Thus, if one can tune the supersaturation level to avoid nucleation while still allowing for growth by monomer addition, having templates off of which tubules grow would improve the specificity of a given target structure without impeding the kinetics (19).

A somewhat surprising result of the origami design is how different the bevel angles of the three different versions of the X triangle are (*SI Appendix*, Table S4). Even though all three of these structures were constructed using the same design principle, resulting in the same length of scaffold for each helix, this approach did not result in the same bevel angles for the different sides. One main difference is that the cross overs between helices had to be placed in different locations to accommodate the different lock-and-key designs. This subtle change may cause unintended torsion within the sides that impacts the relative angles of adjacent sides. One avenue to address this issue would be to use interior supporting struts to add additional length constraints to the system. Another possible issue is that the short (1 to 3 nucleotide) single-stranded DNA segments connecting helices at the vertices might overconstrain the vertices and add stress to the subunit. A design modification that might avoid this issue is to connect the sides at the vertices only in a few locations. Finally, it seems prudent to use existing simulation software, such as oxDNA (44), ENRG MD (45), and mrdna (46), to screen different arrangements of cross-overs to find ones that yield the desired bevel angles.

Overall, our DNA origami colloids represent a powerful platform for programming the assembly of self-limiting architectures. We argue that our ability to program the local curvature with the precision of a few degrees per subunit opens up additional directions in materials design that surpass what is currently possible. Whereas tubules assembled from DNA tiles are made from "floppy" components and therefore prescribed mainly by the interaction specificity encoded in the tile sequences (16–18, 26), our tubule structures can be programmed by both interaction specificity and geometrical specificity. As we showed, these two paradigms can play important complementary roles in self-limited assembly. Geometric specificity can enable economical designs that require only a few subunit species and interaction specificity can improve the accuracy of assembly by eliminating off-target structures. Therefore, we anticipate that being able to prescribe both mechanisms of self-limited assembly, together with the ability to make subunits with ever more complex geometries (47, 48), will allow access to an expanded library of self-assembled structures with interesting material applications. Examples include two-dimensional (2D) lattice-like membranes for patterning or separations (21, 49), spherical shells for encapsulation and delivery (24), fibers or length-limited tubules through geometrical frustration (50, 51), and three-dimensional periodic structures for structural coloration (52).

Materials and Methods

Brief descriptions of our experimental methods are provided below. For more detailed methods see *SI Appendix*, section 1.

Assembly of Triangular Subunits. DNA origami subunits are assembled in a one-pot reaction with 50 nM of p8064 scaffold DNA (Tilibit) and 200 nM of each staple strand (IDT; see *SI Appendix* for sequences) in a standard "folding buffer." Standard folding buffers, described previously (31), contain *X* mM $MgCl_2$, 5 mM Tris base, 1 mM EDTA, and 5 mM NaCl (FoB*X*). Reaction solutions are subjected to a thermal annealing cycle in a Tetrad (Bio-Rad) thermocycler. Optimal $MgCl_2$ concentrations and annealing protocols are described in *SI Appendix*, Table S1.

Purification of Subunits. All origami subunits are purified by gel extraction and concentrated by ultrafiltration. We use a 1.5% agarose gel with 0.5× Tris/Borate/EDTA (TBE) buffer, 5.5 mM $MgCl_2$, and 0.5× SYBR-safe (Invitrogen). Custom-made gel combs that can hold 0.2 mL per well were used to increase the throughput. The folded solution is mixed 5:1 with loading dye (30% wt/vol Ficoll 400, 0.1% wt/vol bromophenol blue, 3× TBE) and run at 110 V for 2 h. We remove the monomer band with a razor blade and dice it into small pieces. Gel pieces are placed in a Freeze 'N Squeeze spin column (Bio-Rad) and kept at −20 °C for 5 min and then spun down for 5 min at 13 krcf. The subnatant is concentrated by ultrafiltration with 0.5 mL Amicon 100-kDa filters. Amicon filters are first equilibrated by centrifuging down 0.5 mL of 1× FoB5 at 5 krcf for 7 min, after

which the flow-through is removed. The DNA origami solution is added up to 0.5 mL and centrifuged at 14 krcf for 15 min, and then the flow-through is removed. This process is repeated until all of the DNA origami solution has been filtered. Finally, we place the filter upside down over a new Amicon tube and centrifuge at 1 krcf for 2 min. The DNA origami concentration of the final solution is measured using a Nanodrop (Thermo Scientific).

Self-Assembly of Tubules. Purified subunits are assembled in 50-μL mixtures of 1× FoB*X* with a monomer concentration of 10 nM. The $MgCl_2$ concentration (*X*) is varied from 5 to 30 mM. The assembly solution is pipetted into a capped 0.1-mL strip tube (Rotor-Gene), which is subsequently placed into a 0.2-mL strip tube (Corning) to suppress evaporation and condensation within the tube. Tubes are loaded into a rotating incubator (Roto-Therm; Benchmark Scientific) at 40 °C for 1 wk.

Negative Stain TEM. Assembly samples are incubated on glow-discharged FCF400-Cu TEM grids (Electron Microscopy Sciences) for 60 to 120 s. Grids are then stained with 2% aqueous uranyl formate solution with 20 mM NaOH for up to 30 s before blotting on filter paper and using vacuum suction to remove excess fluid. Images of the grids are acquired on an FEI Morgagni TEM operated at 80 kV with a Nanosprint5 CMOS camera (AMT) at magnifications between ×8,000 and ×20,000. Tomograms of grid samples are acquired on a Tecnai F20 TEM with an field emission gun run at 200 kV with a Gatan Ultrascan 4k × 4k CCD camera. Tilt series were observed at a magnification of ×32,000 from −50° to 50° in 2° increments. Subsequent analysis is performed using Etomo (IMOD) (53).

Cryo-Electron Microscopy. Higher concentrations of DNA origami are used to prepare cryo-EM grids, summarized in *SI Appendix*, Table S3. Samples are placed on glow-discharged C-flat 1.2/1.3 400-mesh grids (Protochip). Plunge freezing of the grids in liquid ethane is performed with an FEI Vitrobot with sample volumes of 3 μL, blot times of 5 to 8 s, a blot force of −1, and a drain time of 0 s at 20 °C and 95% humidity. All cryo-EM images were acquired with a Tecnai F30 TEM with the field emission gun electron source operated at 300 kV and equipped with an FEI Falcon II direct electron detector at a magnification of ×39,000. Single-particle acquisition was performed with SerialEM. The defocus was set to −2 μm for all acquisitions with a pixel size of 2.87 Å.

Image processing was performed using RELION-3 (32). Contrast-transfer-function (CTF) estimation was performed using CTFFIND4.1 (54). After picking single particles we performed a reference-free 2D classification from which the best 2D class averages were selected for processing, estimated by visual inspection. The particles in these 2D class averages were used to calculate an initial 3D model. A single round of 3D classification was used to remove heterogeneous monomers and the remaining particles were used for 3D autorefinement and postprocessing. A summary of the cryo-EM reconstructions is shown in *SI Appendix*, Table S3. All postprocessed maps are deposited in the Electron Microscopy Data Bank.

Epifluorescence Imaging of Tubules. To dye our samples, we incubate our assemblies with YOYO-1 dye (Invitrogen) at room temperature for at least 0.5 h in a solution of 5 nM DNA origami, 500 nM YOYO-1 dye, and 1× FoB, at the same $MgCl_2$ concentration as that of the assembly. We pipette 1.6 μL of the solution onto a microscope slide that has been cleaned with Alconox, ethanol (90%), acetone, and deionized water and subsequently plasma cleaned. After deposition, a plasma-cleaned coverslip is placed on top to create a thin liquid layer. Samples are then imaged on a TE2000 Nikon inverted microscope with a Blackfly USB3 (FLIR) camera.

Data Availability. Data are available upon request. The dataset consists of thousands of very large electron micrographs that cannot be easily stored in an online repository. The cryo-EM data from this study have been deposited in the Electron Microscopy Data Bank with the following accession codes: EMD-26847, EMD-26848, EMD-26849, and EMD-26850 (55–58).

ACKNOWLEDGMENTS. We acknowledge Don Caspar for sparking an interest in the self-assembly of cylindrical tubules. We thank Botond Tyukodi, Rees Garmann, and Farzaneh Mohajerani for helpful discussions; Thomas Gerling for experimental support; and Ali Aghvami, Mike Rigney, and Berith Isaac for technical support with electron microscopy. TEM images were prepared and imaged at the Brandeis Electron Microscopy facility. This work is supported by the Brandeis University Materials Research Science and Engineering Center, which is funded by the NSF under Award DMR-2011846. D.H. acknowledges support from the Masason Foundation. W.B.R. acknowledges support from the Smith Family Foundation.

Author affiliations: [a]Martin A. Fisher School of Physics, Brandeis University, Waltham, MA 02453; [b]Department of Polymer Science and Engineering, University of Massachusetts, Amherst, MA 01003; and [c]Department of Physics, Technical University of Munich, 80333 Munich, Germany

1. D. L. D. Caspar, A. Klug, Physical principles in the construction of regular viruses. *Cold Spring Harb. Symp. Quant. Biol.* **27**, 1–24 (1962).
2. J. D. Perlmutter, M. F. Hagan, Mechanisms of virus assembly. *Annu. Rev. Phys. Chem.* **66**, 217–239 (2015).
3. H. Sui, K. H. Downing, Structural basis of interprotofilament interaction and lateral deformation of microtubules. *Structure* **18**, 1022–1031 (2010).
4. R. H. Wade, On and around microtubules: An overview. *Mol. Biotechnol.* **43**, 177–191 (2009).
5. S. Cheng, A. Aggarwal, M. J. Stevens, Self-assembly of artificial microtubules. *Soft Matter* **8**, 5666–5678 (2012).
6. B. T. Wimberly *et al.*, Structure of the 30S ribosomal subunit. *Nature* **407**, 327–339 (2000).
7. R. J. Macfarlane *et al.*, Nanoparticle superlattice engineering with DNA. *Science* **334**, 204–208 (2011).
8. W. B. Rogers, W. M. Shih, V. N. Manoharan, Using DNA to program the self-assembly of colloidal nanoparticles and microparticles. *Nat. Rev. Mater.* **1**, 1–14 (2016).
9. H. Fang, M. F. Hagan, W. B. Rogers, Two-step crystallization and solid-solid transitions in binary colloidal mixtures. *Proc. Natl. Acad. Sci. U.S.A.* **117**, 27927–27933 (2020).
10. M. He *et al.*, Colloidal diamond. *Nature* **585**, 524–529 (2020).
11. M. F. Hagan, G. M. Grason, Equilibrium mechanisms of self-limiting assembly. *Rev. Mod. Phys.* **93**, 025008 (2021).
12. Z. Zeravcic, V. N. Manoharan, M. P. Brenner, Size limits of self-assembled colloidal structures made using specific interactions. *Proc. Natl. Acad. Sci. U.S.A.* **111**, 15918–15923 (2014).
13. W. M. Jacobs, A. Reinhardt, D. Frenkel, Rational design of self-assembly pathways for complex multicomponent structures. *Proc. Natl. Acad. Sci. U.S.A.* **112**, 6313–6318 (2015).
14. Y. Ke *et al.*, DNA brick crystals with prescribed depths. *Nat. Chem.* **6**, 994–1002 (2014).
15. J. D. Halverson, A. V. Tkachenko, DNA-programmed mesoscopic architecture. *Phys. Rev. E Stat. Nonlin. Soft Matter Phys.* **87**, 062310 (2013).
16. P. W. K. Rothemund *et al.*, Design and characterization of programmable DNA nanotubes. *J. Am. Chem. Soc.* **126**, 16344–16352 (2004).
17. P. Yin *et al.*, Programming DNA tube circumferences. *Science* **321**, 824–826 (2008).
18. B. Wei, M. Dai, P. Yin, Complex shapes self-assembled from single-stranded DNA tiles. *Nature* **485**, 623–626 (2012).
19. A. M. Mohammed, R. Schulman, Directing self-assembly of DNA nanotubes using programmable seeds. *Nano Lett.* **13**, 4006–4013 (2013).
20. W. Liu, J. Halverson, Y. Tian, A. V. Tkachenko, O. Gang, Self-organized architectures from assorted DNA-framed nanoparticles. *Nat. Chem.* **8**, 867–873 (2016).
21. G. Tikhomirov, P. Petersen, L. Qian, Programmable disorder in random DNA tilings. *Nat. Nanotechnol.* **12**, 251–259 (2017).
22. G. Tikhomirov, P. Petersen, L. Qian, Fractal assembly of micrometre-scale DNA origami arrays with arbitrary patterns. *Nature* **552**, 67–71 (2017).
23. K. F. Wagenbauer, C. Sigl, H. Dietz, Gigadalton-scale shape-programmable DNA assemblies. *Nature* **552**, 78–83 (2017).
24. C. Sigl *et al.*, Programmable icosahedral shell system for virus trapping. *Nat. Mater.* **20**, 1281–1289 (2021).
25. J. B. Bale *et al.*, Accurate design of megadalton-scale two-component icosahedral protein complexes. *Science* **353**, 389–394 (2016).
26. H. Shen *et al.*, De novo design of self-assembling helical protein filaments. *Science* **362**, 705–709 (2018).
27. T. E. Videbæk *et al.*, Tiling a tubule: How increasing complexity improves the yield of self-limited assembly. *J. Phys. Condens. Matter* **34**, 134003 (2022).
28. T. Gerling, K. F. Wagenbauer, A. M. Neuner, H. Dietz, Dynamic DNA devices and assemblies formed by shape-complementary, non-base pairing 3D components. *Science* **347**, 1446–1452 (2015).
29. Y. Yoshimura, "On the mechanism of buckling of a circular cylindrical shell under axial compression" (Tech. Memo. 1390, National Advisory Committee for Aeronautics (NACA), Washington, DC, 1955).
30. R. K. F. Lee, B. J. Cox, J. M. Hill, An exact polyhedral model for boron nanotubes. *J. Phys. A Math. Theor.* **42**, 065204 (2009).
31. K. F. Wagenbauer *et al.*, How we make DNA origami. *ChemBioChem* **18**, 1873–1885 (2017).
32. J. Zivanov *et al.*, New tools for automated high-resolution cryo-EM structure determination in RELION-3. *eLife* **7**, e42166 (2018).
33. M. Kube *et al.*, Revealing the structures of megadalton-scale DNA complexes with nucleotide resolution. *Nat. Commun.* **11**, 6229 (2020).
34. S. Whitelam, R. L. Jack, The statistical mechanics of dynamic pathways to self-assembly. *Annu. Rev. Phys. Chem.* **66**, 143–163 (2015).
35. F. Kilchherr *et al.*, Single-molecule dissection of stacking forces in DNA. *Science* **353**, aaf5508 (2016).
36. A. Kuzyk *et al.*, DNA-based self-assembly of chiral plasmonic nanostructures with tailored optical response. *Nature* **483**, 311–314 (2012).
37. A. Briegel, M. Pilhofer, D. N. Mastronarde, G. J. Jensen, The challenge of determining handedness in electron tomography and the use of DNA origami gold nanoparticle helices as molecular standards. *J. Struct. Biol.* **183**, 95–98 (2013).
38. R. Phillips, J. Kondev, J. Theriot, H. G. Garcia, N. Orme, *Physical Biology of the Cell* (Garland Science, 2012).

39. W. Helfrich, J. Prost, Intrinsic bending force in anisotropic membranes made of chiral molecules. *Phys. Rev. A Gen. Phys.* **38**, 3065–3068 (1988).
40. C. Heussinger, M. Bathe, E. Frey, Statistical mechanics of semiflexible bundles of wormlike polymer chains. *Phys. Rev. Lett.* **99**, 048101 (2007).
41. H. Fang, B. Tyukodi, W. B. Rogers, M. F. Hagan, Polymorphic self-assembly of helical tubules is kinetically controlled. *Soft Matter* **18**, 6716–6728 (2022).
42. D. Chrétien, R. H. Wade, New data on the microtubule surface lattice. *Biol. Cell* **71**, 161–174 (1991).
43. J. Roostalu, T. Surrey, Microtubule nucleation: Beyond the template. *Nat. Rev. Mol. Cell Biol.* **18**, 702–710 (2017).
44. T. E. Ouldridge, A. A. Louis, J. P. Doye, Structural, mechanical, and thermodynamic properties of a coarse-grained DNA model. *J. Chem. Phys.* **134**, 02B627 (2011).
45. C. Maffeo, J. Yoo, A. Aksimentiev, De novo reconstruction of DNA origami structures through atomistic molecular dynamics simulation. *Nucleic Acids Res.* **44**, 3013–3019 (2016).
46. C. Maffeo, A. Aksimentiev, MrDNA: A multi-resolution model for predicting the structure and dynamics of DNA systems. *Nucleic Acids Res.* **48**, 5135–5146 (2020).
47. P. W. K. Rothemund, Folding DNA to create nanoscale shapes and patterns. *Nature* **440**, 297–302 (2006).
48. S. M. Douglas *et al.*, Rapid prototyping of 3D DNA-origami shapes with caDNAno. *Nucleic Acids Res.* **37**, 5001–5006 (2009).
49. J. A. Millan, D. Ortiz, G. van Anders, S. C. Glotzer, Self-assembly of Archimedean tilings with enthalpically and entropically patchy polygons. *ACS Nano* **8**, 2918–2928 (2014).
50. G. M. Grason, Perspective: Geometrically frustrated assemblies. *J. Chem. Phys.* **145**, 110901 (2016).
51. B. Tyukodi, F. Mohajerani, D. M. Hall, G. M. Grason, M. F. Hagan, Thermodynamic size control in curvature-frustrated tubules: Self-limitation with open boundaries. *ACS. Nano.* **16**, 9077–9085 (2022).
52. K. Michielsen, D. G. Stavenga, Gyroid cuticular structures in butterfly wing scales: Biological photonic crystals. *J. R. Soc. Interface* **5**, 85–94 (2008).
53. J. R. Kremer, D. N. Mastronarde, J. R. McIntosh, Computer visualization of three-dimensional image data using IMOD. *J. Struct. Biol.* **116**, 71–76 (1996).
54. A. Rohou, N. Grigorieff, CTFFIND4: Fast and accurate defocus estimation from electron micrographs. *J. Struct. Biol.* **192**, 216–221 (2015).
55. D. Hayakawa *et al.*, cryo-EM data for "Geometrically programmed self-limited assembly of tubules using DNA origami colloids." Electron Microscopy Database. https://www.ebi.ac.uk/emdb/search/EMD-26847. Accessed 5 October 2022.
56. D. Hayakawa *et al.*, cryo-EM data for "Geometrically programmed self-limited assembly of tubules using DNA origami colloids." Electron Microscopy Database. https://www.ebi.ac.uk/emdb/search/EMD-26848. Accessed 5 October 2022.
57. D. Hayakawa *et al.*, cryo-EM data for "Geometrically programmed self-limited assembly of tubules using DNA origami colloids." Electron Microscopy Database. https://www.ebi.ac.uk/emdb/search/EMD-26849. Accessed 5 October 2022.
58. D. Hayakawa *et al.*, cryo-EM data for "Geometrically programmed self-limited assembly of tubules using DNA origami colloids." Electron Microscopy Database. https://www.ebi.ac.uk/emdb/search/EMD-26850. Accessed 5 October 2022.